BIOMEDICAL ENGINEERING

Carnegie Mellon University

2013 Summer Undergraduate Research Program (SURP) Research Poster Presentations

July 24, 2013

University Center, Rangos 2

Noon to 2:00 PM

Support of the 2013 SURP was provided by the Carnegie Institute of Technology and Merck & Co., Inc.

Comparison of Stromal Vascular Fraction vs. Cultured Adipose Derived Stem Cells for Construction of Tissue Engineered Blood Vessels

Katelyn M. Bruce[1], Jeffrey T. Krawiec[1,3], Lauren E. Kokai[2], Antonio D'Amore[3], William R. Wagner[3], J. Peter Rubin[2,3], David A. Vorp[1,2,3]

Departments of Bioengineering[1], Plastic Surgery[2], and McGowan Institute for Regenerative Medicine[3], University of Pittsburgh, Pennsylvania

Introduction: Cardiovascular disease is one of the leading causes of death in the U.S. and current clinical revascularization techniques possess limitations of intimal hyperplasia and thrombosis. However, tissue engineered blood vessels (TEBVs) have shown promise in developing blood vessel grafts improving upon these limitations. Previously, the Vorp lab has created TEBVs seeded with human adipose derived stem cells (ADSCs) and transplanted them within a rat model. These ADSCs proved to have the ability to generate a native-like blood vessel at the site of the graft curing the damaged rat artery. However these cells require *in vitro* expansion which poses many FDA barriers and concerns of cellular transformation.

Adipose tissue is unique in that it provides a plentiful and easily isolated source of cells, of which ADSCs are a subpopulation. This freshly isolated population, known as the stromal vascular fraction (SVF), is also comprised of a rich source of endothelial cells, endothelial progenitor cells, T cells, B cells, and macrophages. Potentially this tissue could be harvested from the patient bedside during surgery and used to construct a TEBV directly instead of being used to isolate and culture ADSCs.

The objective of this study is to analyze the difference between SVF seeded TEBVs and cultured ADSC TEBVs to determine any major differences in cell types comprising the TEBV as this could directly impact the functionality of this heavily cellular dependent therapy. We hypothesize that the SVF will be a possible substitute for the ADSCs within the scaffold, and that the SVF will contain a less purified population of cells than the ADSCs. If this proves to be true, SVF could potentially be used to quickly construct TEBVs with no cell culture required. With the use of immuno-fluorescent chemistry the two types of seeded scaffolds were compared in terms of the types and numbers of cells present. These results will serve as a preliminary study to testing a rat model with SVF seeded TEBVs.

Materials and Methods: SVF was obtained from thigh and abdominal adipose tissue and liposuction of young (Age: 33, 38, 43), healthy female patients under the guidance of the Rubin lab. The isolated SVF was seeded into bilayered poly(ester urethane)urea (PEUU) scaffolds created in the Wagner lab. Scaffolds were seeded using our custom rotational vacuum seeding device and were then cultured for two days in a spinner flask to allow for cell attachment and spreading. A fraction of the SVF was plated and carried out for three passages to obtain cultured ADSCs and each passage was seeded into a scaffold. Cross sections of each of the fixed scaffolds were cut via a cryo-microtome and placed onto gelatin coated slides for analysis. Immunofluorescence staining, with appropriate cell markers (CD4 for T cells, CD20 for B cells, CD31 for endothelial cells, CD34 for endothelial progenitor cells, and CD68 for macrophages) was used to analyze the contents of the scaffolds. Cell count analysis was done using Fiji ImageJ software as well as NIS Elements to obtain a count of the cells present within each cross section.

Results and Discussion: SVF proved to successfully be seeded into PEUU scaffolds producing a TEBV with no cell culture required. SVF seeded TEBVs showed positive cell markings for CD31 (endothelial cells) and CD34 (endothelial progenitor cells). Endothelial cells made up 26.51% and 41.28% of cells in the SVF and ADSC passage 0 seeded scaffolds respectively. Endothelial progenitor cells made up 28.45% and 11.63% respectively. The SVF seeded scaffolds showed no T cells, B cells, or macrophages. Through immunofluorescence staining, the cultured ADSCs showed positive markings for CD31 and CD34. The positive count of CD31 stayed relatively steady up until passage 2. However, the positive count of CD34 decreased as the ADSCs advanced in passage. By passage 3, the cultured ADSCs showed no positive cell markings. Overall, the use SVF and ADSCs to seed scaffolds make TEBVs with different cell types and amount of cells present.

Conclusions: The presence of SVF within the TEBV allows for an increase in the number of endothelial cells and endothelial progenitor cells present. The presence of these cells defines the major differences between SVF and cultured ADSCs. Seeding of SVF or cultured ADSCs prior to passage 2 of culture would show positives markings for endothelial cells and endothelial progenitor cells. However, the richest sources of those cells are seen in the SVF TEBVs seeded directly after isolation. Future work will focus on *in vivo* studies using SVF seeded TEBVs

within a rat model, to determine if SVF TEBVs are a treatment option for cardiovascular patients in need of a new blood vessel.

Acknowledgements: Carnegie Mellon University Department of Biomedical Engineering and Dr. Conrad Zapanta

Traction force microscopy of 3T3 fibroblasts on 2 μm features

Jeffrey C. Chen, Stephanie S. Chang, Yu-li Wang
Department of Biomedical Engineering, Carnegie Mellon University

Introduction: Recently, mechanical signaling has been shown to regulate cell behavior such as spread area, migration, and apoptosis. In one mode of mechanical signaling, adherent cells exert forces, termed traction forces, on the extracellular substrate. Previous studies have shown that traction force generation is linearly correlated with cell geometry and focal adhesion size (Rape et al., *Biomaterials* 2011). Furthermore, it has been shown that cells treated with nocodazole, a drug that depolymerizes microtubules, exhibit an increase in traction force and focal adhesion size. This project investigates whether focal adhesion growth is necessary for the increase in traction force generation. A recently developed micropatterning technique will allow us to control both cell spread area as well as confine focal adhesion size. Traction forces will be quantitatively measured by analyzing the displacement of beads that are embedded in soft gels on known elastic modulus.

Materials and Methods: We confined NIH 3T3 cells on a "half-frame" pattern: a 50 x 50 μm square consisting of a 2 μm thick frame adjacent to a filled-in rectangle. A polydimethylsiloxane (PDMS) stamp was fabricated using standard soft photolithography techniques. Briefly, SPR-220.3 photoresist was exposed to UV light under a photomask with the half-frame pattern and developed using MF-26A developer. The PDMS stamp was incubated with 0.1% bloom gelatin oxidized with 3.6 mg/mL sodium periodate. Polyacrylamide gels embedded with 0.2 μm green fluorescent beads were made following the method published Rape et al. NIH-3T3 fibroblasts allowed to spread overnight, and phase and fluorescent images were taken before and after cells were detached from the gel with 0.05% Trypsin-EDTA. Vector maps of bead displacement were created with the DIM software (Y.L. Wang, Carnegie Mellon University). Traction stresses were calculated and force maps were generated using LIBTRC 2.0 (M. Dembo, Boston University).

Results and Discussion: We were able to control substrate elasticity and micrometer-scale presentation of extracellular ligands for cell adhesion using the micropatterning technique described. By using specified amounts of acrylamide and bis-acrylamide, we were able to fabricate hydrogels with an elastic modulus of approximately 5.8 kPa. The oxidation of gelatin allowed us to directly pattern polyacrylamide gels such that the protein is covalently linked to the surface of the hydrogel. Electrostatic interactions between the oxidized protein and the fluorescent beads further allow us to visualize the micropattern. The 95% traction stress of single cells spread on the half-frame pattern was 2.6×10^4 Pa. After treatment with 10 μM nocodazole, the 95% traction stress increased to 3.2×10^4 Pa (N = 25).

Conclusions: Traction forces increase after nocodazole treatment even when focal adhesion sizes are confined on 2 μm features. This result suggests that other mechanisms may play a role in the cellular response to microtubule depolymerization. Such mechanisms may involve upregulation of the actomyosin contractility system independent of those that control focal adhesion growth.

Acknowledgements: I would like to thank Dr. Yu-li Wang for giving me the opportunity to perform research in his cell mechanics lab. I also want to thank the three Ph.D. students, Stephanie Chang, Stephanie Wong, and Jian Zhang, all of whom patiently guided me throughout the research project. Lastly, I would like to acknowledge Kristin Galuska and Dr. Conrad Zapanta for coordinating SURP. This work was supported by Carnegie Mellon University SURP awarded to JCC.

Isolation of a single chain variable fragment for TNF-alpha neutralization

Brittany Couture, Emily Friedrich, Saumya Saurabh, Yehuda Creeger, Marcel Bruchez, Newell Washburn.

Introduction: TNF-alpha is a proinflammatory cytokine produced mostly by activated macrophages during the inflammation process in wound healing. It is a homotrimer with three 17kDa subunits, and acts as an upstream regulator for other cytokines also involved in inflammation. TNF-alpha increases local vascular permeability and recruits more macrophages and neutrophils to the wound site. Several autoimmune disorders, including rheumatoid arthritis, Crohn's disease, and psoriasis, have been treated by inhibiting TNF-alpha, most commonly with monoclonal antibodies. Currently available inhibitors include Remicade (infliximab) and Humira (adalimumab), however because these are entire antibodies, they can cause unwanted side effects.

Antibody fragments are becoming more useful as binding reagents for treating inflammatory diseases and cancers due to their small size and increased tissue permeability. A single chain variable fragment (scFv) is a protein that contains only the variable heavy and variable light chains of an antibody. These are linked together by a flexible peptide. ScFvs are useful because they contain the specificity region of the antibody, where a specific antigen will bind, and eliminate some of the potentially harmful side effects. The objective of this study was to produce an scFv that is specific to rat TNF-alpha, and will bind to and inhibit it effectively, for eventual use in inhibiting TNF-alpha in a rat burn model.

Materials and Methods: A yeast surface display library was used to express a range of scFvs and determine which would bind to TNF-alpha. The display libraries incorporate a DNA vector into the yeast genome, and once induced, display the protein on the surface of the cell. Two tags are included in the sequence: a hemagglutinin (HA) tag, and a c-Myc antibody tag. The c-Myc tag will show whether or not the entire scFv is present. The yeast library contained around 10^9 cells that each expressed a different mutation of the inserted protein sequence. Fluorescence-activated cell sorting was used to sort out the yeast cells that bound to rat TNF-alpha from those that did not. To accomplish this, rat TNF-alpha was labeled with Alexa 633. Once the desired fluorescent signal was detected, the cell would be sorted out from the rest of the stream.

Results and Discussion: The modified yeast cells were sorted a total of 5 times to produce an enriched population. On the fifth sort, three distinct populations were chosen to gate on, 2 anti-c-Myc positive, and one just on Alexa 633 (Figure 1a). Approximately 100 cells were dropped onto a plate, and 19 colonies grew. One colony was imaged under a fluorescence microscope to confirm binding of TNF-alpha (Figure1b), meaning the cell will fluoresce around the outside.

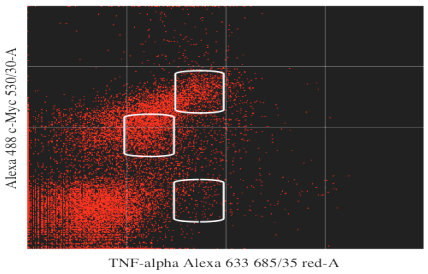

(a)

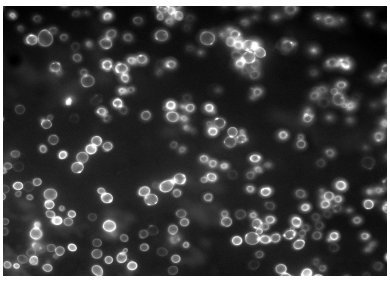

(b)

Figure 1. (a) Three populations chosen to grow on plate, 2 anti-c-Myc positive (upper boxes), and one just Alexa 633 (lower box), (b) Fluoscent image of induced cells with TNF-alpha and Alexa 633, confirmation of expression of the scFv and binding to TNF- alpha

Conclusions: After several sorting steps, a relatively pure sample was obtained of genetically modified yeast cells that display scFvs with a positive binding affinity for rat TNF-alpha. 19 colonies were dropped and grown onto an agar plate. The next steps are to sequence the colonies on the plate, choose a varitety of the sequenced colonies for protein production, determine TNF-alpha neutralization with selected scFvs using a macrophage neutralization assay, and compare binding affinities. The protein selected will display the best binding affinity to and neutralization of TNF-alpha.

Geometric characterisation of cerebral aneurysms for prediction of rupture risk.

Conor Fitzgerald, Ling Zhan, Hong Zhang, Jessica Zhang, Kenji Shimada

Introduction: Cerebral aneurysms are a disease of the cardiovascular network within the brain due to blood vessel dilations where the vessel wall becomes weak which leades to the formation of bulges. They often occur near a bifurcation and will continue to weaken the wall and increase the size of the bulge which may lead to a rupture of the aneurysm. In the event of a rupture there is a 40% chance of mortality, and a further 25% chance of death due to complications in the following six months. The purpose of this project has been to use geometric statistics to predict rupture risk of the sample aneurysms. The first project that was undertaken was a fully automatic method to identify an aneurysm as an alternative to relying on manual segmentation of all aneurysms. This is an important step because it will speed the process of identifying the desired geometric statistics. The second project has been a multi-scale approach to identifying rupture risk by incorporating these geometric statistics with patient information, fluid stress analysis and solid stress analysis of the aneurism samples.

Materials and Methods: The aneurysms were to be automatically segmented using a solution based on conditional random field, cost-sensitive gentle adaboost and random sample consensus. A group of manually segmented meshes were used as training data where all vertices were labeled as being either healthy vessels or aneurysm. The method then fit a quadratic surface to the aneurysm bulb to further increase accuracy and improves the smoothness of the segmentation. 60 samples were selected from the repository to be segmented using these new methods and were compared to manually segmented samples. These samples were segmented out separately using the program paraview to identify the aneurysm and store the information of all vertices on the aneurysm sac. Geometric statistics such as vessel diameter, sac volume, sac surface area, neck diameter and the aspect ratio were taken from these segmented models. Those statistics were combined with patient and case information such as patient age, sex, aneurysms location and rupture status, which were taken from the repository and several machine learning techniques attempted to handle this information in order to get a preliminary accuracy reading. Currently information is being gathered about the fluid stresses experienced within the surrounding vessel network using ANSYS CFX software to calculate the maximum wall shear that is experienced. Additionally CUBIT software is being used to prepare the aneurysms for a solid mechanics stress simulation. Theses stress values will eventually also be incorporated into the statistics being analyzed to predict rupture risk.

Results and Discussion: For automatic segmentation before quadrtatic surface fitting, the average overall accuracy of the method is 92.83%±1.09 and the average sensitivity was % 93.46%±1.19%. After the quadratic surface fitting was applied the accuracy increased to 95.73%±4.24% and the sensitivity increased to 97.53%±1.89%. Several machine-learning techniques were used and the maximum accuracy achieved was 62% and was achieved by using a Linear regression model.

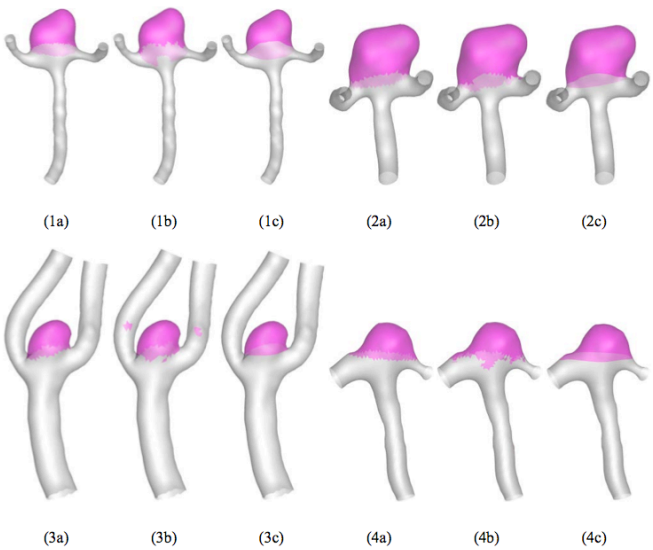

Figure 1: (a) Manually labeled surface of thirty aneurysms. Magenta represents an aneurysmal dome and grey represents a healthy vessel; (b) classification results; and (c) segmentation results after quadratic surface fitting.

Conclusions: These results demonstrate a robust method of automatically segmenting the aneurysm sacs. Future work is to be done in order to separate the aneurysm from a larger network of vessels. The current rupture risk analysis is less accurate than desirable but work will continue to be done to gather information on the stresses experienced in order to improve this accuracy.

Single Wall Carbon Nanotubes as Delivery Vehicles for Hydrophobic Molecules for Imaging and Therapy

Gina Lu[1,2], Patrick D. Boyer[1], Brian D. Holt[2], Mohammad F. Islam[3], Kris N. Dahl[1,2]
[1]Department of Chemical Engineering, [2]Department of Biomedical Engineering, [3]Department of Materials Science and Engineering, Carnegie Mellon University, Pittsburgh, PA

Introduction: Bovine serum albumin (BSA) is a natural surfactant-like protein with several hydrophobic pockets. The hydrophobic pockets of proteins have been utilized to disperse small molecules such as dyes and drugs and have also proven effective in creating high yield dispersions of single wall carbon nanotubes (SWCNTs). Previous work in the group has shown our length-fractionated (~150 nm) SWCNTs dispersed using BSA easily fit within typical endosomes and phagosomes and they readily enter cells in large amounts (up to 50 million SWCNTs per cell for macrophages). Furthermore, because of the high coverage of BSA molecules per SWCNT (~30 BSA molecules), SWCNTs-BSA represent ideal vectors that can transport difficult to deliver hydrophobic molecules inside cells in elevated amounts for increased therapeutic effect. In this work, we investigate the delivery of fluorescein as a model hydrophobic molecule which is easily visualized in cells using standard microscopy techniques. We will exploit the surfactant-like behavior of BSA protein to interact with both fluorescein and SWCNTs and hypothesize that intracellular enzymes will degrade the BSA on SWCNT surfaces thereby releasing large quantities of the pre-loaded hydrophobic molecules into the cytoplasm of cells.

Materials and Methods: Equal molar solutions of BSA and fluorescein in water were mixed and allowed to reach equilibrium. The BSA-fluorescein complex was used to disperse individual SWCNTs at 10:1 BSA:SWCNTs by weight through a procedure of probe tip sonication and subsequent ultracentrifugation to remove bundles. The binding and release of fluorescein from the BSA hydrophobic pocket was tracked using absorbance and fluorescence spectroscopy. *In vitro* fluorescein release was tested using both enzymatic (trypsin) degradation and heat (>70C) denaturation of the protein. Finally, a model macrophage cell line with high proteolytic activity was treated with 10 μg/mL SWCNTs-BSA-Fluorescein for 24 hours. The intracellular prescence of SWNCTs and delivery of fluorescein was quantified using a combination of NIR and visible fluorescence imaging.

Results and Discussion: In the presence of BSA, fluorescein showed both an increase in absorbance magnitude and a 10 nm red shift in peak location. In addition, fluorescein fluorescence was also decreased by 50%. Both of these changes indicate the entrapment of fluorescein within the BSA hydrophobic pocket. Disruption of the protein structure via thermal denaturation and trypsin, resulted in an increase in fluorescence, which shows that the fluorescein is being released from the BSA hydrophobic pocket. A dispersion of SWCNTs using the BSA-Fluorescein complex resulted in individual SWNCTs indicated by the sharp peaks in absorbance and near-infrared (NIR) fluorescence that can only come from individually dispersed nanotubes. In vitro thermal and enzymatic degradation of SWCNTs-BSA-Fluorescein shows similar increases in fluorescein fluorescence indicating that fluorescein can be released from the BSA pocket even when BSA-Fluorescein is used to disperse SWCNTs. Finally, when SWCNTs-BSA-Fluorescein was added to J744A.1 model macrophage cells, intracellular release of fluorescein and fluorescence was observed, though with significantly less mean intensity than that of BSA-Fluorescein alone, potentially due to the artifact of quenching from the SWCNTs.

Conclusions: SWCNTs have been shown to be capable of being delivery vectors for small hydrophobic drugs. By using BSA to disperse the nanotubes, small hydrophobic drugs can also bind to BSA and be release into the cytoplasm through either thermal denaturation or enzymatic digestion. Future studies include quantifying intracellular release kinetics, NIR light triggered release of molecules to improve delivery control, as well as investigating the delivery of other fluorophores and drugs including rhodamine derivaties.

Acknowledgements: I would like to thank Dr. Kris Dahl and Dr. Mohammad Islam for their guidance throughout this project. In addition, I'd like to thank Patrick Boyer for his assistance throughout all of the experiments and Brian Holt for his help with the imaging and spectroscopy. Furthermore I'd like to acknowledge Dr. Abbe N. de Vallejo from Children's Hospital of Pittsburgh UPMC and Dr. Stephen F. Badylak from University of Pittsburgh and McGowan Institute for Regenerative Medicine. Finally, I'd like to thank Kristin Galuska and Dr. Conrad Zapanta for giving the opportunity to participate in the SURP program.

Determining the direction of radial head translation during maximal forearm supination

Lindsey Milisits, Carnegie Mellon University

Introduction: Approximately one third of all elbow fractures occur at the radial head. Depending on the severity of the fracture, it may require surgical fixation, excision, or replacement. At the elbow, the radial head articulates with the humeral capitellum and the proximal ulna. This structure allows for flexion and extension at the radioulnar joint as well as pronation and supination movement. By quantifying the degree of translation of the radial head during supination , researchers will have a better understanding of the kinematics in the elbow. This information can help determine appropriate treatment for radial head fractures and aid in the design of radial head replacements.

Materials and Methods: Using standard radiograph equipment, a DICOM file of a test subject's right forearm relaxed and flexed at 90 degrees was obtained. Another x-ray of the subject's arm while applying maximal supination contractions yet maintaining a neutral pronation/supination position at 90 degree flexion angle was also imaged. The subject grasped a strength tester handle and applied a supination force while his arm stayed in position. The strength tester reported the force being applied to ensure each trial output the same amount of torque. A total of 6 x-ray images were taken, 3 with the forearm relaxed and 3 with the forearm loaded. Two metal blocks of known dimensions were also imaged in each x-ray to provide a basis for scaling and converting pixels to inches. Using MatLab, two coordinate systems for measuring the degree and direction of movement of the radial head were created. In both systems, the centroid of the radial head and capetellum were located. One system measured the position of the capitellum relative to the radial head (radial head frame) and the other measured the position of the radial head relative to the capitellum (capitellum frame). Two separate axes were created by consistently choosing a point in the radial shaft just before the tuberosity or humeral shaft respectively. Data was collected in both radial head coordinates and in capitellum coordinates. The difference in position of the radial head between the relaxed images (no supination) and the loaded images (maximal supination loading) were calculated and averaged for each coordinate system.

Results and Discussion: Both reference frames agreed that the direction of translation of the radial head during supination is upwards and to the left towards the humerus. However, the distances measured in the x and y directions for the radial head reference frame were more consistent between each of the 3 trials then the distances measured in the capitellum reference frame. This is because the point in the radial shaft that served as the x-axis for the radial frame was more consistently chosen then the point in the humeral shaft due to its close proximity. Thus, measuring the position of the capitellum with respect to the radial head was determined to be the better method for measuring radial head translation. There was a rather high variability between measurements for each reference frame so an average across trials was determined. However, analysis from the radial head reference frame suggests an average translational movement of the radial head of 0.9068 mm upwards and 0.6477 mm towards the humerus.

Conclusions: After analysis, both methods of measuring radial head translation conclude that the radial head moves upward and towards the humerus while applying maximal supination force. Measuring the position of the capitellum with respect to the radial head was determined to be the better method for measuring radial head translation. An accurate magnitude of radial head movement was not calculated but an average between trials was determined. The method for calculating radial head movement has been refined multiple times in order to more accurately measure the translation with minimal sources of error. Care will be taken in future experiments with more test subjects to keep the source of error in the x-ray images to a minimum. The elbow flexion angle of 90 degrees will be more properly maintained. A circular disk instead of a rectangular block may be used to more accurately determine a scale from inches to pixels. Overall, this experiment provided a basis for calculating radial head translation and has provided significant insight as to the direction of movement during supination which will be useful in future clinical applications.

Acknowledgements: I would like to thank Mark Miller for coordinating and directing this project. I would also like to thank Will Anderton for assisting me. This research opportunity was provided to me by The Department of Biomedical Engineering, Summer Undergraduate Research Program, Carnegie Mellon University.

Effects of antibiotics and platelet rich plasma (PRP) based biomaterials on C2C12 cells

Mariah Ondeck. Carnegie Mellon University, Carmell Therapeutics. Pittsburgh, PA.

Introduction: The newest way of helping to heal tissue injuries is to utilize all plasma, and concentrate the platelets to form plasma-based biomaterials (PBM)[1], which accelerates healing. Antibiotics, such as gentamicin and vancomycin are currently used prophylactically to avoid bacterial infections at injury sites and improve patient outcomes, yet they can cause severe damage to the surrounding tissue through their cytotoxic effects. C2C12 cells are progenitor cells derived from mouse skeletal muscle cells that can be affected when there are repairs or infections in the muscle. Testing the antibiotics in conjunction with the new plasma therapies on the C2C12 cells will help to advance new therapies for muscle injury by not only facilitating the repair process but also potentially reducing the cytotoxic effects of antibiotics on healthy cells.

Materials and Methods: The primary method to determine whether cell viability can be improved in the presence of antibiotics in PBM media is via the MTT assay, which measures cell viability. PBM media is produced by first spinning whole blood to remove red blood cells. Next, calcium chloride is added to form a powder that can then be mixed with complete Dulbecco's Modified Eagle Medium (DMEM) growth media.[1] The MTT assay is performed by seeding 5,000 C2C12 cells/well (passage 9-19) in a 96-well plate. After 24 hours, the cells are treated with media containing the antibiotic of choice. Finally, the cells are incubated with the assay dye for four hours. After incubation, a stop solution is added and viability is determined by comparing the absorbance of replicated treatment wells to those of an untreated (control) group.

Results and Discussion: Focusing on the effects of gentamicin, the cell viability is much greater with the use of PBM media than without (Fig 1). This does not support the hypothesis that the use of PBM media protects against the cytotoxic effects of gentamicin, but does prove that the addition of PBM media helps to keep more cells alive. Further testing is required to confirm the conclusion of the effects of vancomycin in PBM media, but the data collected thus far shows that there is no significant difference between PBM media and complete DMEM media.

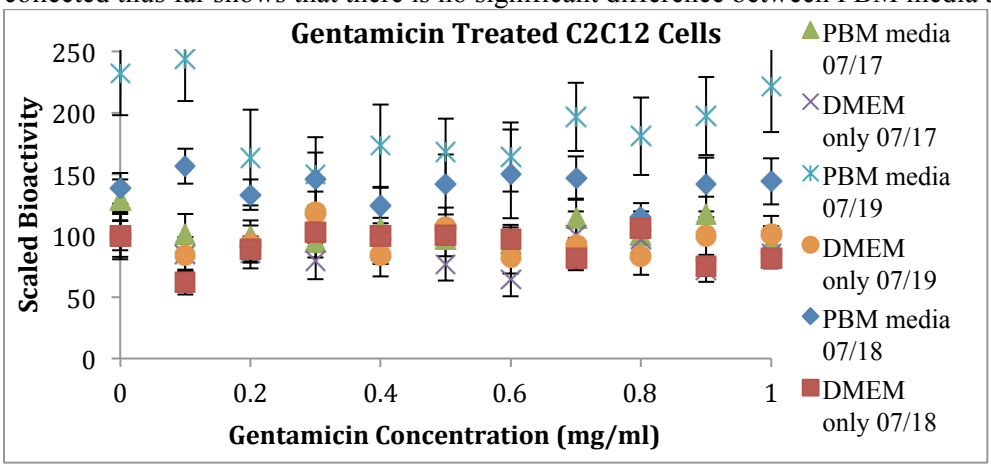

Figure 1. This graph displays cell viability over a range of gentamicin concentrations from 0 to 1 mg/ml. The cells treated with PBM media versus DMEM media have a higher viability.

Conclusion: This data shows that gentamicin and vancomycin did not induce cytotoxicity in C2C12 cells at the dosages tested; however, treatment with PBM media alone could have potential positive effects on stem cells required for muscle repairs when used in conjunction with gentamicin. Interestingly, PBM media alone was not able to enhance cell viability in C2C12 cells treated with vancomycin. While vancomycin may not induced cytotoxicity in the cell line, it may have limited the ability of PBM media to enhance viability. Also, C2C12 cells are just one type of muscle stem cell; additional muscle cell lines should be tested for a stronger conclusion regarding the effects on muscles, such as muscle-derived stem cells. In the future, antibiotic concentrations could be increased to induce a greater cytotoxic response and further validate the protective effects of PBM on cell viability.

References: 1. Jason DS et al., Disruptive Science and Technology, 2012, Volume 0.

Characteristic of Fibronectin with Varying pH Environment

Shigeto Ono, John Szymanski, Adam Feinberg
Regenerative Biomaterials and Therapeutics Group
Dept. of Biomedical Engineering, Dept. of Materials Science and Engineering, Carnegie Mellon University

Introduction: Fibronectin (FN) is a glycoprotein that is critical component of the extracellular matrix (ECM)[1] during embryonic development and wound healing.. FN has a large variety of binding domains for integrins, ECM proteins, growth factors, and self-assembly that ultimately plays a role in cell processes such as adhesion, proliferation, and differentiation. Some of these binding sites are cryptic and require FN to be mechanically unfolded to become exposed. To date, little is known about the effect of pH on the mechanical stability of FN. Interestingly wound and cancer microenvironments are accompanied by an acidic pH and could potentially alter the ability for cryptic sites to become exposed. In this study, we measured the effect of pH on the ability of FN to refold from an unfolded state. We used a surface initiated assembly[2] technique in which FN was microcontact printed in an unfolded state on a thermally sensitive surface. Dissolving the surface allows FN to release from the surface and refold in solution. In this study we measured the rate and extent of FN refolding in acidic, neutral, and basic environments to determine the effect of pH on the refolding properties of FN.

Materials and Methods: Microcontact printing process[2] was conducted in this experiment. Cover slips were coated with 10% poly(N-isopropylacrylamide) (PIPAAm) solution. 184 Sylgard PDMS stamps with a 200x20 µm pattern were coated with FN solution with a concentration of 50ug/mL. The dried FN coated stamps were placed onto the PIPAAm coated coverslip. The releasing process was conducted with three different solutions: deionized water (pH from 5.21 to 5.38), SE buffer (pH 8.6), and PBS (pH 7.2). A Nikon Ecplipse TS100 microscope was used to record and analyze the release.

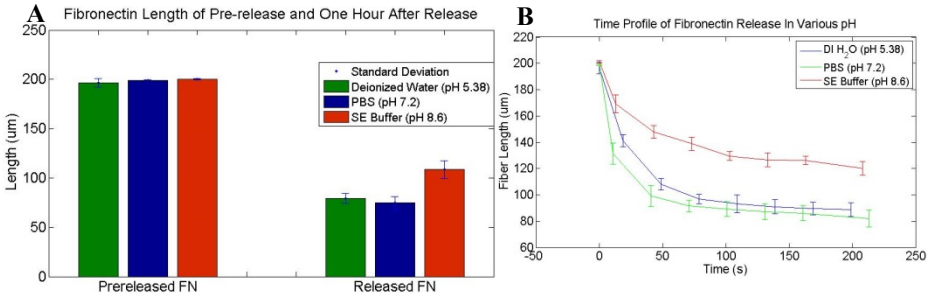

Figure 1 (A): The fibronectin fiber lengths were analyzed in 30 second intervals for each sample to make a FN release profile. Figure 2 (B): FN during Prerelease and an hour after release were analyzed to determine the final length of the contracted fibers.

Results and Discussion: FN nanofibers were released in acidic (pH = 5.38), neutral (pH = 7.2) and basic (pH =8.3) solutions. An example of the release process is shown in Figure 1c. By analyzing the contour length of FN nanofibers after release, the fibers in basic solution (pH 8.3) contracted (refolded) the least compared to neutral (pH = 7.2) and acidic (pH =5.8) solutions. Figure 1A depicts the length of the FN nanofibers pre-release and after an hour in solution post-release. Plotting the length as a function of time qualitatively indicates the similarity in the rate of contraction in neutral and acidic environments (Figure 1B). The similarity in fiber length of pH 5.38 and 7.2 correlate to the pH in which FN functions critically, such as a wound environment and in the bloodstream (pH of 7.4).

Conclusion: The release profiles identified how pH affected the refolding properties of FN. The acidic and neutral environments had similar fiber lengths after refolding while basic environments had greater fiber lengths. A possible future experiment may be investigating the functionality of these fibers with various pH, including attachment to integrin embedded in an ECM scaffold. This can portray how mechanical property of FN affects its utility.

Acknowledgements: I would like to thank Adam Feinberg, Ph.D, Carnegie Mellon University Department of Biomedical Engineering, and John Szymanski for guidance and assistance throughout this project.

References: 1) Pankov, Roumen, and Kenneth M. Yamada. "Fibronectin at a Glance." *JCS* 115 (n.d.): 3861-863. 2) Feinberg AW and Parker KK, Nano Lett, 2010, 10, 2184-91.

Simulation of Needle Insertion into Brain Tissue for Safe Needle Steering

Yixing Shi [1,2], Craig Lehocky [1], and Cameron N. Riviere [1,2,3]
[1]Dept. of Biomedical Engineering, [2]Dept. of Mechanical Engineering, [3]The Robotics Institute
Carnegie Mellon University Pittsburgh, PA, USA
yixings@andrew.cmu.edu

Introduction

Deep needle insertion into brain tissue is a common medical procedure for diagnoses and treatment, such as administering chemotherapeutic agents and brain tumor biopsy. Straight rigid needles are often inserted in a linear fashion from the surface towards the area of interest deep in the brain. Recently, some research groups have been developing needles that can be steered along non-linear paths, enabling the needle to reach the target while avoiding critical structures between the entry point and the target.

Bevel-tipped flexible needles naturally curve during insertion due to the asymmetry of the tip, and the curvature amount is dependent on needle and tissue properties. Needle steering is accomplished by rotating the needle as it is inserted to change direction. The amount of curvature in any particular direction is controlled by rotating the needle in a duty-cycled fashion as it is inserted. However the force that the needle imparts on surrounding tissue need to be taken into account to avoid tissue damage.

The goal of this study is to accurately model the interactions between tissue and needle under small deformations. The resulting model will be used to design a customized bevel-tipped needle that curves as much as possible while imparting forces that are well below the amount that would damage the tissue.

Methods

The software package ABAQUS was used to develop the finite element analysis simulations. In this set of experiments, a 3D representation of a 0.13mm radius needle was inserted into a 7mm by 7 mm by 3.5 mm block of brain tissue with all forces at equilibrium at the initial step. The brain tissue was modeled as a linear elastic material with a Young's modulus of 7 kPa and a Poisson's ratio of 0.475. The needle's material was simulated as nitinol, a flexible nickel-titanium alloy with a Young's modulus of 50 GPa and a Poisson's ratio of 0.3.

Simulations were conducted for various combinations of insertion speed, bevel tip radius, and bevel angle. The simulations were coupled Eularian - Lagrangian Analysis, with the needle as the solid Lagrangian part, and the brain tissue modeled as a viscoelastic Eulerian fluid.

Simulations were performed for three bevel angles: $10°, 20°,$ and $30°$; three bevel tip fillet radii: 0.025mm, 0.05mm, and 0.1mm; as well as three needle insertion velocities (0.25mm/s, 0.5mm/s, and 1.0 mm/s). The needle was inserted into the tissue a total of 0.1mm, the time periods for each of the simulations are 0.4s, 0.2s, and 0.1s for each respective velocity.

Results

The stress and strain values were taken from the element that experienced the maximum of both values at the very end of the simulation. The tissue stress results are well under the estimated stress damage threshold for brain tissue (120kPa). However, not all needle profiles met the maximum allowable strain threshold. All needle insertions at the insertion speed of 1mm/s induced tissue strain that would cause damage. Only at the needle insertion speed of 0.25mm/s did all needle profiles produce acceptable strain rates. However, the largest bevel tip radius of 0.1mm produced the smallest strain rate out of the other profiles.

Conclusion

The results show that the biggest factor in tissue safety during needle steering is the speed of needle insertion. In general, the needle parameter that leads to the greatest tissue damage is a small bevel tip fillet radius. The effect of bevel angle on tissue damage is somewhat inconclusive. At faster speeds of insertion, a smaller bevel angle produced a smaller strain, whereas at other speeds, a larger bevel angle produced smaller strain.

There are some discrepancies between the data generated by the 3D simulations and the previously done 2D simulations. For example, previously there was no correlation between the stress-strain values and the needle insertion speed. However in the 3D simulations, the stress-strain values increased proportionally with speed of insertion. The simulated tissue also underwent some type of impact-generated recoil around the area of insertion, resulting in the stress strain values taking on a wave like shape that may have impacted its accuracy.

Bulk phase transitions of thermoplastic materials via embedded microfluidic vascularization

Mike Standish, Aditya Balsubramanian, Dr. Christopher Bettinger Carnegie Mellon University

Introduction: Thermoplastics are polymers capable of drastically altering their material properties without changing phase. Specifically, the elastic modulus of a thermoplastic can change so drastically that the material shifts from being rigid and brittle to very flexible within a small increase of temperature. Such a phenomenon can be observed within its glass transition temperature and melting point -whereby past the glass transition temperature, the crystalline structure of the material changes enough to cause such property changes while maintaining the overall phase. In addition, the transition is reversible, with the thermoplastic reverting back to its previous state when cooled. For this unique ability, thermoplastics have been viewed as a focus material for a new age of machinery. Robotic arms and wings capable of transforming structure could enable new innovations in both the performance and longevity of devices. This project explores how the uses of thermoplastics could be executed by passing water at different temperatures through embedded channels within the material to initiate the glass transition shift.

Materials and Methods: The thermoplastic of choice was VeroWhite (Manufactured by Stratasys) due to the alignment of its material properties to the needs of the project, ability to be printed three dimensionally to exact specifications, and availability. In order to properly model the heat transference occurring during the vascularization of water through the channels the thermal conductivity, and coefficient of thermal expansion at constant pressure of the material were needed. In addition, four geometries with .5 mm thick channels were generated to test the role of vascularization with the speed of material transition. Prior to modeling heat transference, experiments that involved a differential scanning calorimeter were run on the VeroWhite to determine its thermal conductivity. Vascularization of water through the four geometries was then modeled to determine how quickly the glass transition temperature could be reached.

Results and Discussion: The thermal conductivity experiments yielded the values of .093 W/(m•K) for samples 3D printed horizontally and .120 W/(m•K) for samples printed vertically. Based on experiments with other materials, the source of this experimental method claimed it has a 27% accuracy of validly finding the thermal conductivity. This was further confirmed with a repetition of the experiment using Teflon that was accurate within 13.5% of literature values. Using the thermal conductivity values, density, and coefficient of thermal expansion at constant pressure, the modeling of heat transfer for each geometry was possible. By combining this model with experimental data for the surface temperature outside each thermoplastic geometry, effects of convective cooling were accurately verified and incorporated into the model. The model and experimental data from a three point bending test performed on the VeroWhite as it was heated produced a final model which represents the change in elastic modulus versus response time from onset of water vascularization (Figure 1).

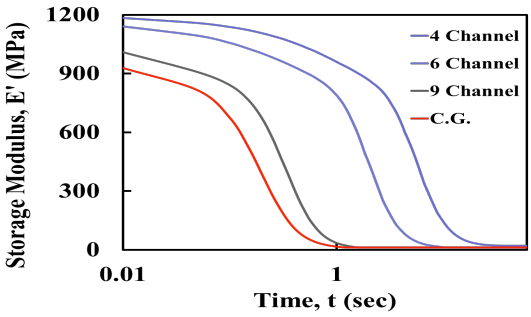

Figure 1. Theoretical Storage Modulus versus time for all four geometries. Dip in elastic modulus indicates point of glass transition temperature.

Conclusions: Of the four geometries, the response time from when vascularization begins to glass transition varies from approximately .3 to 10 seconds. Considering how quickly a machine may need such a transition to occur, the results indicate that for the two fastest geometries –complex and 9-channel- the method of vascularizing water through the material in a practical scenario is valid. Any machine whose functionality would benefit from being able to transform parts from rigid to rubber-like within less than a second would have great use for this technology. A future study for this experiment could involve construction of a robotic arm that grasps objects by using its material glass transition temperature to encapsulate and then harder around the target object.

Design of neuron culture platforms for investigating neurodegenerative diseases

Eric Volk, Dept. of Biomedical Engineering; Dept. of Mechanical Engineering, Carnegie Mellon University

Introduction

Neurodegenerative diseases, such as Alzheimer's, Huntington's, and strokes are poorly understood in their causes. Different complications for neuronal cell culture methods have hindered progress in related investigations. Due to the sensitive and partially understood association of degenerative neuronal cells with such diseases, knowledge of the pathophysiologies of various neurodegenerative diseases is lacking. Campenot chambers, a culture platform commonly used for neurons, has been ineffective in culturing CNS (central nervous system) neurons, such as those from the spinal cord, that are linked to such diseases. Additionally, *in vivo* studies are subject to physiological varations, making them inherently costly as well. A novel culture platform, through use of soft lithography and microfluidics, has been shown in multiple studies to be an effective, versatile, inexpensive, and reliable alternative. These culture platforms, i.e. microfluidic devices, have exceptional potential for neurobiological studies. In designing them, however, a great deal of care is necessitated for their viability, and to avoid common defects that other platforms and methods possess. This study focused on such design considerations, specifically those needed for experiments on axon transport, injury, and regeneration. Of the multiple resulting designs, some were purposed for further experimentation on neurons and overall platform design refinement, others for direct experimentation elucidating axonopathies underlying neurodegenerative diseases.

Materials and Methods

A microfluidic device is composed of a PDMS structure and an adherent substrate. The size, shape, and stiffness of the PDMS structure are dictated chiefly by a photomask design, of which is representative of the culture platform features. The transparent photomask is placed atop a glass coverslip coated with SU-8 photoresist, and then exposed to UV light. A photoresist developer is used to remove photoresist in excess of the features, and PDMS molds can then be produced from the resulting master templates. Differences in existing methods for layering the photoresist or UV light exposure time and intensity can yield vast differences in the three-dimensional features in the microfluidic device (e.g. fluid channel height, or thickness). For culturing CNS neurons, designs typically consist of microchannels (in the order of 10μm wide, 5μm tall, and of varying length) connected in parallel to two larger channels (in the order of 1mm wide, 100μm tall, and several mm long) at the ends of which circular reservoirs (in the order of 8mm diameter) are connected. A similar design was incorporated in the photomask used in this study. The utilization of 10μm width, 450μm height microchannels have been demonstrated to induce axonal growth along such channels, isolated from soma and dendrites. This isolation permits well controlled studies of axon transport mechanisms, axotomy, axonal processes, axon injury, and axon regeneration. As the channels are in parallel, many experiments can be run simultaneously. Through a difference in cell medium volume between reservoirs on each side of the microchannels, laminar flow can be established through a hydrostatic pressure gradient, fluidically isolating one side from the other for superior experimental control. Other properties of both this design and the use of PDMS allow for reproducible experiments, and templates derived from the photomask and photoresist allow for repeated used.

Results and Discussion

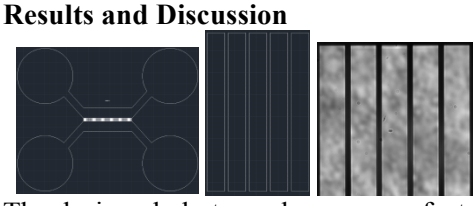

Figure 1. (left) AutoCAD Design of two-compartment microfluidic device. **(middle)** Magnified view of microchannels joining microfluidic device compartments. **(right)** View of photomask microchannels using a wide view microscope. Not to scale.

The designed photomask was manufactured by Photo Sciences Incorporated onto a transparency mask (Figure 1, right), and can be used for experimentation and observation of axotomy and axonopathies.

Conclusions

Althought the design of microfluidic devices, and similar PDMS structures, for CNS neuron culturing hasmuch room for refinement, such devices have strong potential for investigating neurodegenerative diseases.